Sustainable Energy & Fuels

ROYAL SOCIETY OF CHEMISTRY

PAPER

View Article Online
View Journal | View Issue

Cite this: *Sustainable Energy Fuels*, 2024, **8**, 3726

Thermally integrated photoelectrochemical devices with perovskite/silicon tandem solar cells: a modular approach for scalable direct water splitting†

Angela R. A. Maragno,[a] Adina Morozan,[b] Jennifer Fize,[b] Michel Pellat,[c] Vincent Artero,*[b] Sophie Charton*[a] and Muriel Matheron‡*[d]

Direct solar water splitting appears to be a promising route to produce hydrogen, avoiding competition for electricity with other important economic uses. Halogenated hybrid perovskites recently enabled the demonstration of efficient and potentially low-cost photoelectrochemical cells and PV-coupled electrolysers, reaching high efficiencies but so far limited to a small active area of a few mm^2, in the case of perovskite/silicon tandem solar cells. Here, we show the added value of integrating a thermal exchanger into the system thanks to additive manufacturing, providing a thermally integrated photoelectrochemical cell (IPEC) with performance doubled compared to the device without any heat exchanger (from 3.3 to 8% STH). In addition, we develop a modular approach to scale-up this concept from 7.6 to 342 cm^2, highlighting statistical variations in the efficiency of single integrated photoelectrochemical cells and their origin. We conduct an outdoor stability test for 72 hours, achieving a STH performance of 6.3%, and investigate the causes of device degradation through the easy disassembly of the integrated photoelectrochemical devices. We identify the interface between the perovskite layer and p-layer as critical for achieving stable photoelectrochemical devices integrating perovskite/silicon tandem solar cells.

Received 25th April 2024
Accepted 26th June 2024

DOI: 10.1039/d4se00547c

rsc.li/sustainable-energy

1 Introduction

The conversion of solar energy and water into chemical energy *via* the production of hydrogen is a topic that has attracted substantial interest for years. Many different technologies have been investigated so far to produce hydrogen from sunlight and water. To reach maturity, such technologies should be at the same time (i) efficient (in terms of solar-to-hydrogen (STH) efficiency), (ii) stable under intermittent operation and over years of operation, and (iii) scalable, which means that they should rely on earth-abundant materials and cost- and energy-effective processes.[1] The main challenge is to achieve high STH efficiency with low-cost materials (light absorbers, catalysts, and membranes) and to overcome barriers that limit the scalability and the stability of such new technologies.

Several architectures exist and are often grouped into three categories: (i) photocatalytic (PC) cells, (ii) photoelectrochemical (PEC) cells, and (iii) photovoltaic cells coupled to electrolysers (PVEs), with or without a power management system. In the latter case, integrated photoelectrochemical cells (IPEC cells) are single devices with an area-matched photoabsorber and electrocatalyst.[2] When calculating the levelized cost of hydrogen (LCOH) of the various possible configurations, having in mind the target of $ 2 per kg set by the U.S. Department of Energy (DOE) to compete with hydrogen derived from fossil sources,[3,4] no system obviously takes the lead. In addition to the immaturity of certain technologies, introducing uncertainty into the cost calculations, the outcomes of these studies are highly dependent on the location where the system will be implemented, the expected lifetimes, the cost of materials (which can fluctuate, particularly as the result of potentially unpredictable geopolitical events), and local regulations or incentives. For example, some studies show that concentrated solar power achieves the lowest cost, provided it is implemented in locations with high irradiance levels.[5] Regarding the use of a power converter, the literature reports contradictory results. One study, for example, claims that lower costs would be

[a]*CEA, DES, ISEC, DMRC, Univ. Montpellier, Marcoule, France. E-mail: sophie.charton@cea.fr*

[b]*Univ. Grenoble Alpes, CNRS, CEA, IRIG, Laboratoire de Chimie et Biologie des Métaux, 38000 Grenoble, France. E-mail: vincent.artero@cea.fr*

[c]*Univ. Grenoble Alpes, CEA, LITEN, DTNM, 38000 Grenoble, France*

[d]*Univ. Grenoble Alpes, CEA, LITEN, Campus INES, 73375 Le Bourget du Lac, France*

† Electronic supplementary information (ESI) available. See DOI: https://doi.org/10.1039/d4se00547c

‡ Present address: Univ. Grenoble Alpes, CEA, LITEN, DTCH, 38000 Grenoble, France.

obtained for PVE systems fitted with a power converter,[6] while another states that the use of power converters has no significant effect on cost.[5]

However, there is a consensus that the demand for electricity will increase in the coming years. All scenarios promote electrification, whenever possible, to decarbonize our economy.[7] Therefore, competition for electricity availability and greater constraints on grid stability are expected to emerge. With this perspective, producing renewable fuels, such as hydrogen, without drawing electricity from the grid, seems particularly relevant.[8] In order to advance the deployment of these systems and subsequently refine the cost analysis, it is important to carry out practical demonstrations, whether they involve scalability validations or preliminary tests in a real environment. This will provide clearer knowledge of the concrete issues that need to be overcome.[9–11]

Here, we focus on water splitting devices based on halogenated hybrid perovskites, emerging as efficient low-cost light absorbers, assembled into integrated photoelectrochemical (IPEC) cells and modules.[2] Halogenated perovskite materials have become attractive candidates for efficient and cheap light harvesting applications, such as photovoltaics, photocatalysis and photoelectrochemistry. They reconcile efficiency and cost, although more needs to be done in terms of long-term stability. Since 2015, halogenated perovskites have been coupled to low band-gap absorbers in tandem solar cells in order to reduce thermalization losses in the high-energy region of the solar spectrum. This approach has enabled rapid rise in the efficiency of power conversion,[12] with a 33.9% record recently reported for perovskite/silicon tandems, hence surpassing the theoretical limit for a single junction solar cell.§ Recent papers report the association of a perovskite/silicon tandem solar cell with an electrolysis device, demonstrating high STH efficiency. The first demonstration came in 2019 with a STH efficiency of 17.52%.[13] A STH efficiency of 18–19% followed in early 2020[14,15] and then close to 20% (ref. 16 and 17) and finally above 21% since 2021.[18–20] According to theoretical studies, the maximum achievable STH efficiency for a tandem system is above 25%,[21,22] provided that materials with optimal band gaps can be synthesized. The tunability of the band gap of perovskites explains the growing interest in these materials from the solar fuels community.[23]

To date, studies on the combination of perovskite/silicon tandem solar cells and electrolysers, or on photoelectrodes based on perovskite/silicon absorbers, have all been carried out on a small scale and under laboratory conditions. The largest active surface area[14] and the longest stability test[20] already reported under controlled indoor conditions are 1.42 cm^2 and 102 h, respectively. In the present work, instead of targeting for record performance for single devices, we adopted a practical approach towards real-life implementation. We used perovskite/silicon tandem solar cells with a significantly larger active area (7.6 cm^2), collected repeatability data on more than fourty-five IPEC cells, included a gas separation function in the electrolyser (which had only been demonstrated once in previous work[19]), and assessed stability under outdoor conditions. In addition, we integrated an internal heat exchanger to transfer heat from the solar cell to the electrolyser to improve efficiency. The benefits of thermal integration have already been demonstrated, in the case of PEC cells under concentrated illumination,[24] for PEC architectures comprising mature single junction absorbers such as silicon and copper indium gallium selenide (CIGS)[25] and for silicon-based triple junctions. For instance, in the latter case, the loss in the multi-junction efficiency at high temperature was balanced by the improved kinetics in the electrolyser, and optimal conditions were observed close to 50 °C.[26] Simulation studies performed on perovskite/silicon tandem solar cells also show that thermal coupling is beneficial.[27] For perovskite-based absorbers, this approach could be particularly relevant, as heat and its combination with illumination, even non-concentrated, are known to have deleterious effects on their lifetime.[28]

To achieve this, we chose a modular approach for the IPEC fabrication, allowing easy assembly and disassembly of the components, so that rapid material variations can be assessed (initially and after ageing) and scaled through numbering-up. IPEC cells, which can separate the H_2 and O_2 gases produced and integrate a heat-exchanger to boost performances, were first built and tested on a small scale (7.6 cm^2 active surface area)[29] to assess the gain in STH efficiency from thermal integration. Then, we designed IPEC modules assembling nine IPEC cells (68.4 cm^2 active surface area).[30] Five of these IPEC modules were finally combined, with a total active surface area of 342 cm^2, enabling a more in-depth study of the performance dispersion. Stability was assessed in the laboratory during "day–night" cycles, and outdoors during 72 hours of autonomous operation.[31] Dismantling the modules enabled the components to be characterized after ageing and the identification of the limits to be overcome to improve lifetime.

2 Materials and methods

2.1 Components description

2.1.1 Tandem solar cell fabrication and encapsulation

Silicon bottom cell fabrication. Silicon heterojunction bottom cells are processed starting from commercially available n-type float-zone (100) oriented both side polished silicon wafers (chemical mechanical polishing), 4 inch size, with a thickness between 260 and 300 μm and a resistivity between 1 and 5 Ω cm. Wet cleaning with hydrofluoric acid (HF) and hydrochloric acid (HCl) is performed to remove native oxides and contaminants, before the deposition of intrinsic amorphous silicon layers (a few nanometers thick) on both sides of the wafer, by plasma enhanced chemical vapour deposition (PECVD) at 200 °C with SiH_4 and H_2 gases. Doped amorphous silicon layers are then deposited by PECVD on each side of the wafer, adding phosphine gas (PH_3) for the n-doped a-Si:H layer and diborane (B_2H_6) for the p-doped a-Si:H layer. The back-side electrode, made of indium tin oxide (ITO), is then deposited by sputtering. The recombination layer, also made of ITO, is then deposited by physical vapor deposition (PVD). The thickness and carrier

§ Longi claims 33.9% efficiency for perovskite-silicon tandem solar cells – pv magazine International (https://pv-magazine.com).

density are adjusted to provide enough recombination centers in the bulk of the layer while maintaining an acceptable transparency in the infrared range.

Perovskite top cell fabrication. Silicon heterojunction bottom cell wafers are laser cut to 5 × 5 cm^2 size. A 200 nm layer of silver is then thermally evaporated to form the back-side electrode. The electron transport layer (ETL) is prepared from a commercially available tin oxide (SnO_2) nanoparticle colloidal suspension diluted in deionized water. Perovskite and hole transport layers are prepared in a glovebox the day before deposition, as follows. Formamidinium lead iodide ($FAPbI_3$), lead bromide ($PbBr_2$) and cesium iodide (CsI) mother solutions are prepared by dissolving lead iodide (PbI_2) and formamidinium iodide (FAI) in an *N*,*N*-dimethylformamide/dimethylsulfoxide mixture (DMF/DMSO) at 40 °C, $PbBr_2$ in a DMF/DMSO mixture at 40 °C and CsI in DMSO at ambient temperature. The solution of $Cs_xFA_{1-x}Pb(I_{1-y}Br_y)_3$ is prepared the next day, mixing in a vial the $FAPbI_3$, $PbBr_2$ and CsI solutions so that $x = 0.05$ and $y = 0.17$. The hole transport layer (HTL) is prepared as follows: poly(triaryl amine) (PTAA) is dissolved in toluene and lithium bis(trifluoromethylsulphonyl)imide (Li-TFSI) in acetonitrile at ambient temperature, and then Li-TFSI solution and 4-*tert*-butylpyridine (*t*BP) are added to the PTAA solution, and the resulting mixture is kept at 65 °C overnight. Right before the top cell fabrication, a 30 min UV–ozone surface treatment is applied to the recombination ITO. The cells are immediately introduced into a glovebox to perform further steps under an inert nitrogen atmosphere. The SnO_2 colloidal suspension is spin-coated on the recombination ITO, followed by annealing at 80 °C for 1 min on a hot plate. The perovskite layer is then deposited by spin-coating, with a chlorobenzene quenching step to promote perovskite crystallization. Annealing is performed on a hot plate at 100 °C for 1 h. The HTL is then formed on top of the perovskite by spin-coating the PTAA solution. The transparent front side electrode is obtained by sputtering at ambient temperature to form a 100 nm thick ITO layer. A 200 nm thick gold grid, thermally evaporated, is finally added. Devices are then stored in the dark in ambient air before use.

Solar cell encapsulation. A conductive metal ribbon (3M 3007 solar tape) is manually pressed on the front and back sides of the solar cell. 5 × 5 cm^2 glass lids are cleaned using acetone, isopropanol and water and dried in an oven for 1 h. An epoxy glue is manually spread over the cells' front side before carefully placing the glass lid on top. The glue thickness is adjusted to around 120 μm thanks to tape separators placed at the cell corners. Crosslinking is then triggered by 400 nm incident photons provided by a DELOLUX source (LED) for 2 min. The cells are stored in the dark and in ambient air before use.

2.1.2 PEM electrolyser. The proton exchange membrane (PEM) electrolyser consists of two current collector plates with flow channels (cathodic and anodic) between which the membrane electrode assembly (MEA) is interposed, on either side of which the gas release reactions take place. All components are placed in an anodic box, which is essential for closing the device and managing water distribution and collection.

Cathodic and anodic plates, as well as the anodic box, are manufactured using 3D printing[32] to maximize the cell's compactness, with metal being replaced by polymer where feasible for the function of the component. This makes it possible to reduce the weight of the cell, develop alternative energy conversion devices and overcome the restrictions of traditional hydrogen manufacturing methods for hydrogen generators. The anodic box is made of polyoxymethylene (POM), a technical thermoplastic. The anodic flow-plate features a machined flow channel consisting of six serpentines, each 1 mm wide, which distribute preheated water evenly over the entire anode surface. The serpentine flow channel is manufactured from polypropylene (PP) by Fused Deposition Modeling (FDM). A 200 nm thick electrically conductive gold layer was deposited on the flow area of the PP plate using the electron-beam physical vapour deposition (EBPVD) technique.

The MEA was prepared using a Nafion NRE-212 membrane (50 μm thick, Alfa Aesar), iridium black (Alfa Aesar) as the anode catalyst with a fixed loading of 5.7 mg cm^{-2}, and a 0.5 mg cm^{-2} 60% Pt-Vulcan/carbon cloth gas diffusion electrode (FuelCellStore) as the cathode. The anode catalyst ink was deposited by drop-casting onto a 12.3 cm^2 area of a decal substrate poly(-tetrafluoroethylene) (PTFE)-coated fiberglass cloth (Plastic Elastomer) until the desired catalyst loading was reached. The cathode electrode and the coated decal substrate were assembled by sandwiching the Nafion membrane and hot-pressing it at 120 °C for 90 s under 5 MPa. The anode catalyst was transferred to the Nafion membrane by peeling off the decal substrate following the hot-pressing process.

The cathodic plate is made of 316L stainless steel by additive manufacturing (AM) using Laser Powder Bed Fusion (LPBF) technology, also known as Selective Laser Melting (SLM). A laser is used to melt and solidify metal powder in a specific area, which is then molded into a layer-by-layer stack. After each cycle, the powder is raked or rolled onto the previous consolidated layer. Thanks to this technique, we were able to integrate thirteen parallel channels into the metal mass. These channels, with their 2.3 mm side, are distributed across the entire width of the plate, the outer face of which is designed to host the solar cell, and thus enable optimum distribution of the water to be preheated. The integrated pin flow channel design, facing the MEA, was chosen because of its enhanced performance compared to "conventional" flow channels due to reduced ohmic resistance.[33]

A Pt-coated titanium grid (254 μm thick, 12.25 cm^2, FuelCellStore) was added on the anode side without pressing during the PEM electrolyser cell assembling. The cell is closed with silicon gaskets (GETELEC), nuts and bolts.

2.1.3 IPEC cell and module. In the IPEC cell, the PEM electrolyser and the perovskite/silicon tandem solar cell (PV) are electrically connected *via* the external surface of their cathode sides. This direct integration is enhanced by the intercalation of an indium sheet between the two sides. The face-to-face contact does not induce any additional series resistance to that measured at the solar cell terminals. To conduct holes to the water oxidation sites, the positive terminal (anode) of the tandem solar cell is connected to the anode of the electrolyser *via* a low-resistivity tin-plated copper ribbon, a silver wire and a platinum wire. Finally, a mask in polyamide 11 (PA11) is

positioned around the PV to precisely define the irradiated surface.

The IPEC module has been developed to integrate nine individual IPEC cells (Fig. S1†). The module anodic box is manufactured in a single piece to optimize thermal integration, limit both the number of steps for fluidic assembly and the risk of leaks. The nine IPEC cells are electrically independent and in series 3 by 3 in terms of fluid management.

Table S1† summarizes the main components of the IPEC cell and module, and their specific features.

2.2 Characterization of efficiency and stability

2.2.1 Photovoltaic efficiency measurement. A class A solar simulator (Oriel 92190, Xe source and AM1.5 filter) is used to simulate solar irradiation in continuous mode. The current–voltage $I(V)$ curves of the illuminated cells are recorded using a Keithley 2602A source measure unit (SMU). Calibration is performed with a standard silicon solar cell (monocrystalline silicon solar cell, WPVS) from Fraunhofer ISE and a spectrophotometer (Aescusoft). The electrical connection of the cells is ensured either by gold probes positioned on the front side and a metal chuck on the back-side, or (in the case of encapsulated devices) using crocodile clamps placed on the metal ribbons. An 8.5 cm^2 mask is used in all cases. Unless otherwise stated, results are not corrected for the shading losses due to metal contacts (estimated to be around 15%).

Acquisitions are monitored with homemade Labview software. Several $I(V)$ sweeps are performed under continuous illumination and under the following conditions, until the efficiency stabilizes: reverse scans (from 2.2 V to − 1.5 V) with one scan every 10 s, steps: 50 mV, dwell time: 20 ms, scan speed: 1.36 V s^{-1}, the number of power line cycles (NPLCs) set to 1, and the cell kept at open circuit between measurements.

2.2.2 Active area measurement. The aperture of each mask was determined using ImageJ software and a calibrated scale for accuracy. The aperture of the standard mask used to characterize the photovoltaic cells (according to 2.2.1) was 8.5 cm^2. The aperture of the mask placed on the solar cells integrated into the IPEC cells was 10.2 cm^2. The active area of the IPEC cells was determined by contrast analysis to identify the area where all layers of the solar cells are present (9.0 cm^2, corresponding to the PVD hard mask), from which the shaded areas are subtracted (Fig. S2†). They have variable surfaces, depending on the alignment of the ribbon in the metallization. On average, a shaded area of 1.4 cm^2 was obtained, leading to an active area of 7.6 cm^2 for the IPEC cells (Table S2†).

2.2.3 (Photo)Electrochemical measurements. The set-up for electrochemical measurements, along with the electrochemical reaction cell, includes two peristaltic pumps (PP1300, WVR), an ultrapure water (Milli-Q) reservoir with a temperature controller (Pilot ONE HUBER circulation thermostat), and a computer-controlled potentiostat (SP-300 Bio-Logic with $a \pm 10$ A/[0, 5] V booster). For a series of specific measurements, two separate water circuits were installed, one to pump water into the internal heat exchanger of the cathodic plate and the other directly to the anodic flow side. Before starting operation and measurement, water was pumped for 30 min into the IPEC cell at a flow rate of 5 mL min^{-1}. A REGLO-CPF digital reciprocated pump with a piston pump-head RH0CKC was used to deliver 17 mL min^{-1} for an IPEC module. A Hioki Memory HiLogger (LR8431-20) and several temperature sensors were used to control the temperature of the various parts of the IPEC cell or module.

The performance of MEAs in the PEM electrolyser was evaluated by recording their polarization curves from 0 to 1.6 V with a scan rate of 10 mV s^{-1}. The curves were *iR*-corrected by automatically carrying out ohmic drop compensation using EC-Lab software through the electrochemical impedance technique (ZIR).

A Solaronix Solar simulator (M205 500-1300 We SN:120125-16; FADEC Software – Multiple Light Engine Version) was used for the photoelectrochemical measurements. The IPEC cell (or the module) is positioned facing the light beam. The IPEC device and the potentiostat are connected in series as follows: the working electrode port of the potentiostat is connected to the top contact (+) of the solar cell, the bottom contact (−) of the solar cell is connected to the cathode (−) of the electrolyser, and the counter electrode port of the potentiostat is connected to the anode (+) of the electrolyser. The reference electrode port of the potentiostat is connected to the counter electrode port in order to measure the current passing through the closed system. No additional potential was applied. Chronoamperometry (CA) measurements were carried out at a fixed irradiation power density (1 sun) and under light/dark cycles.

The operating voltage and current of the tandem integrated in the IPEC cell were measured using a multimeter (RS:123-3245, range 2 V, resolution 1 mV, and error: ± 0.5%).

2.2.4 Gas flow measurements. For single IPEC cells and PEM electrolysers, (photo)electrochemical measurements are coupled with a gas detection device (MilliGascounter type MGC-1 PMMA, RITTER) to quantify the H_2 volume and flow rate. The MGC-1 is specially adapted to small gas flow rates with an error smaller than ± 1% in the range 1 mL h^{-1} to 1000 mL h^{-1}.

Gas flow values for a single IPEC module were estimated from the electrical current, assuming a constant faradaic efficiency of 74% for each cell.

For the assembly of IPEC modules, the H_2 flow-rate was measured with a BROOKS SLA5850S mass flowmeter.

2.2.5 Outdoor stability tests. Outdoor experiments were carried out on IPEC modules tested in the field (Fig. S3†), at the Joint Research Center (JRC) of the European Commission, Ispra (Italy), under conditions close to ISOS-O-1 conditions (with the solar cells delivering their power to the electrolyser). The IPEC modules were tilted 25° against the horizontal and oriented south to optimize the irradiance striking the solar cells. The solar cell $I(V)$ curves were recorded after an ageing test to detect any changes in their performance before/after outdoor exposure. To do so, the solar cells were dismounted from the IPEC modules and measured according to the lab procedure described in 2.2.1. The values of Global Horizontal Irradiance (GHI) were recorded from the ESTI Meteo Tower in Ispra (JRC Ispra ‖ 45° 48′ 43.4′ N–8° 37′ 37.4′ E ‖ altitude: 220 m), positioned approximately 100 m from the IPEC modules.

2.3 Data analysis and calculation of solar-to-hydrogen (STH) efficiency

All calculations have been carried out considering standard conditions of pressure and temperature (25 °C and 1.013 bar), from the Environmental Protection Agency (EPA) and Standard Ambient Temperature and Pressure (SATP) reference.[34]

The STH efficiency is calculated according to the following equation:[35]

$$\mathrm{STH} = \frac{I_{\mathrm{op}} \times E^{\circ} \times \mathrm{FE}}{E_{\mathrm{sun}} \times A} \quad (1)$$

where I_{op} is the operating current in A, E° is the potential (here, 1.23 V), FE is the faradaic efficiency, E_{sun} is the incident solar power in W m^{-2}, and A is the active area of the solar cell in m^2.

Another definition, STH*, is given by the following equation[9] that compares the produced energy in the form of H_2 to the energy of the incident light on the active area of the device:

$$\mathrm{STH}^* = \frac{n_{\mathrm{H_2}} \times \Delta G_{\mathrm{r}}}{E_{\mathrm{sun}} \times A \times t} \quad (2)$$

where $n_{\mathrm{H_2}}$ is the total amount (in mol) of hydrogen produced, ΔG_{r} is the reaction's Gibbs free energy (237 kJ mol^{-1}) of the water splitting reaction at 298 K (corresponding to 1.23 V, the thermodynamic voltage of water splitting), and t (in s) is the duration of the hydrogen production experiment.

For the outdoor experiment in Ispra, to calculate the STH* efficiency, a correction factor was applied to GHI values in order to account for the tilt angle between the IPEC plane and the horizontal plane and obtain the power density striking the IPEC modules. This correction factor, equal to 0.9, was estimated by comparing the calculated horizontal and tilted irradiance values (Fig. S4†).

3 Results and discussion

3.1 IPEC cell features and motivation for thermal integration

Fig. 1 describes the building blocks of the IPEC cell; we integrated a monolithic perovskite/silicon tandem solar cell (Fig. 1b) with an n–i–p architecture on the cathode side of a proton exchange membrane (PEM) electrolyser (Fig. 1a). This allows the water splitting reaction to be driven under illumination, by means of the photovoltage produced by the tandem solar cell. The tandem solar cell is made of a 1.58 eV bandgap halide perovskite absorber sandwiched between charge transport layers (SnO_2 for electrons and doped poly(triaryl amine) (PTAA) polymer for holes) and transparent conducting oxide electrodes, connected in series to a silicon heterojunction bottom cell *via* an indium tin oxide (ITO) recombination layer, which enables the charge recombination of electrons (from the perovskite top cell) and holes (from the bottom cell). Fig. 1c shows the current–voltage $I(V)$ curves recorded under illumination. Typical voltages reached at the maximum power point are of the order of 1.3–1.4 V (Fig. S5†), above the thermodynamic voltage for water splitting (1.23 V).

We built the PEM electrolyser described in Fig. 1a by additive manufacturing to enable the integration of a heat exchanger into the cathodic flow plate and to optimize fluid distribution. The membrane electrode assembly (MEA) is sandwiched between two gaskets and two 3D printed flow plates. A Pt-coated titanium grid improves electrical contact and water distribution at the anode. The anodic flow plate is adapted from the literature,[33,36] where the printed serpentine flow channels facilitate a fast and uniform water distribution. Polypropylene (PP) was selected because of its low cost, flexibility (to facilitate final sealing of the assembly), chemical compatibility with PEM water electrolysis components, and availability from a wide range of suppliers. The cathodic flow plate is a 3D-printed stainless steel monolithic plate[32] with a pin structure designed both to maximize electrical contact with the MEA and to accommodate the gas flow (H_2). We also implemented a heat exchanger in this cathodic flow plate through additional internal channels (see Fig. S6†), which preheats the water (before sending it to the anode) while cooling the tandem solar cell. The stack is assembled in a polyoxymethylene (POM) anodic box and tightened with nuts and bolts. Fig. 1c shows a typical $I(V)$ curve of such a PEM electrolyser.

The operating point of the IPEC cell sits at the crossing point of the $I(V)$ curves of the PEM electrolyser and the solar cell, as shown in Fig. 1c. In general, only the crossing point at 25 °C is considered, whereas in practice under illumination, the device temperature rarely remains at 25 °C. The IR range of the solar spectrum (which is not fully absorbed by the 1.12 eV silicon bottom cell) results in significant heating of the system. For instance, it is known that solar panel temperature can reach at least 60 °C outdoors. In this work, the $I(V)$ curves of tandem solar cells were recorded both on a hot plate after temperature stabilization (near 60 °C) and at room temperature (Fig. 1c), the curves recorded at 60 °C being more representative of the real IPEC working conditions. As the operating temperature increases, even if water splitting reactions are favoured thanks to the reduction in thermodynamic and kinetic barriers, a significant voltage drop is observed in the tandem solar cells, which could prevent reaching a sufficiently high potential for hydrogen production. An ideal situation could be achieved if the PEM electrolyser could operate at 60 °C and the tandem solar cell at 25 °C. In this case, the operating current and therefore the hydrogen production would be maximized (Fig. 1c). These considerations motivated us to integrate a heat exchanger into the electrolyser, as already done in some IPEC cells operating under concentrated illumination.[24]

3.2 Influence of a heat exchanger on IPEC cell efficiency

Fig. 2a shows the path of the water inside the heat exchanger to the anode, and Fig. 2b shows the temperatures recorded along the water circuit, on the tandem solar cell and the cathodic plate, when the IPEC cell was exposed to 1 sun illumination. Several cycles of around 10 h each were performed. The stabilized working temperature of water at the anode (T_4) was *ca.* 40 °C, with the water inlet temperature to the heat exchanger (T_1) always 10 °C lower than the water outlet temperature from the

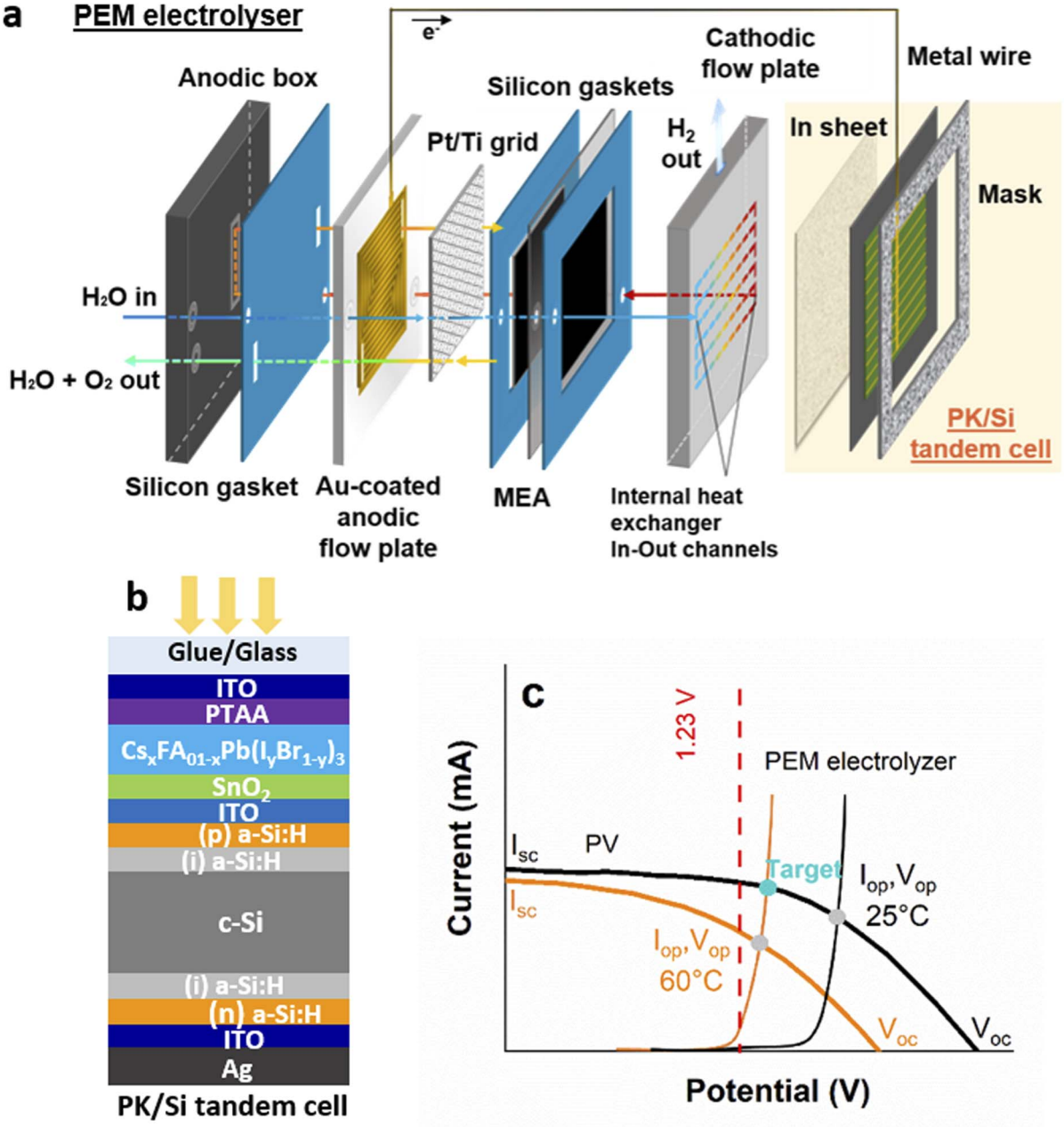

Fig. 1 IPEC cell description (7.6 cm^2 active area) and its operating points as a function of temperature. (a) Scheme of the PEM electrolyser with an internal heat exchanger and perovskite/silicon tandem solar cell integrated on the cathode side. (b) Details of the perovskite/silicon tandem solar cell architecture. (c) Crossing points of the *I*(*V*) curves of the tandem solar cell and the PEM electrolyser operating with water at different temperatures (black: 25 °C and orange: 60 °C).

heat exchanger (T_2), revealing preheating of the water in the exchanger before entering the anode. Equilibrium was reached between the cathodic plate temperature (T_5) and the water outlet temperature from the heat exchanger (T_2). However, the operating temperature of the tandem solar cell (T_6) was around 55 °C, always higher than T_4 and T_5, meaning that in practice the ideal case described in Fig. 1c was not achieved. A more efficient heat exchanger would have to be implemented in order to effectively decrease the temperature of the tandem solar cell to a value equal to or lower than that of the electrolyser. Nevertheless, our strategy was relevant since we observed a heat transfer from the cathodic plate to the anode, resulting in improved efficiency for the IPEC cell, as shown in Fig. 2d and Table 1. The progressive increase in T_1 was explained by the fact that the water outlet at the anode (T_4) was directed to the inlet water tank feeding the cathodic plate.

The performance of the IPEC cell under 1 sun, with and without water flow inside the heat exchanger, is compared in Table 1. The heat exchanger operation (*i.e.*, with water flow) led to an increase in operating current from 46 to 70 mA, with the corresponding hydrogen flow rates of 0.2 to 0.4 mL min^{-1}. As a result, the STH* was more than doubled, from 3.2% to 8.0%.

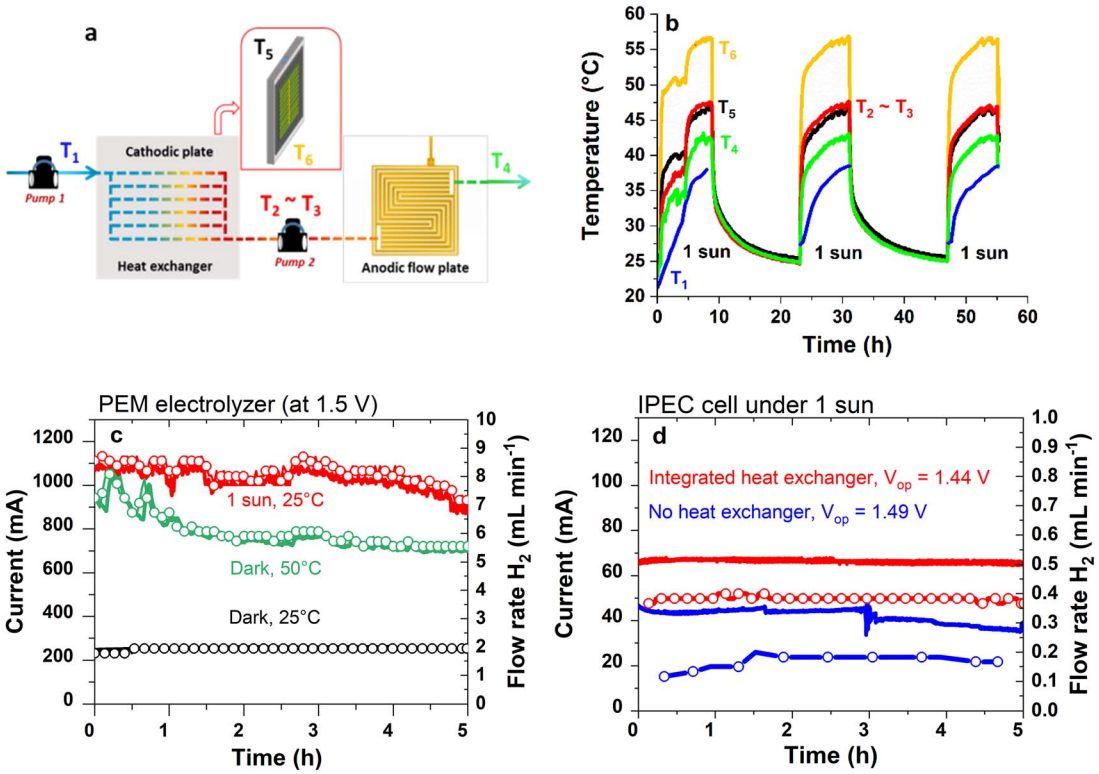

Fig. 2 IPEC cell thermal integration and performance. (a) Detailed scheme of the water circuit in the IPEC cell and (b) recorded temperatures. T_1 (blue): water inlet in the heat exchanger. T_2 (red): water outlet from the heat exchanger. T_3 (red): water inlet in the anodic compartment. T_4 (green): water outlet from the anodic compartment. T_5 (black): temperature of the cathodic plate. T_6 (yellow): temperature of the tandem solar cell. (c) Water splitting current (solid line) and H_2 flow rate (solid line + circles) of the PEM electrolyser under different heating conditions (through the exchanger with water at different temperatures or under illumination). (d) Water splitting current (solid line) and H_2 flow rate (solid line + circles) of the IPEC cell without (blue) or with (red) the heat exchanger.

Table 1 Detailed results of the PEM electrolyser and IPEC cell performance (V_{op} and I_{op}: operating voltage and current recorded at the electrolyser's terminals, t: duration of the hydrogen production, Vol. H_2: corresponding hydrogen volume produced during the experiments of Fig. 2, STH and STH*: solar-to-hydrogen efficiencies calculated using two methods as described in the Materials and methods section, and ** without water flow in the heat exchanger)

	Dark/illuminated mode	Initial inlet water temperature (°C)	V_{op} (V)	I_{op} (mA)	t (h)	Vol. H_2 (L)	STH (%)	STH* (%)
PEM electrolyser	Dark	25	1.50	250	6	0.69	—	—
PEM electrolyser	Dark	50	1.50	800	6	2.41	—	—
PEM electrolyser	1 sun	25	1.50	1000	6	2.94	—	—
IPEC cell**	1 sun	25	1.49	46	5	0.05	3.6	3.3
IPEC cell	1 sun	25	1.44	70	6	0.13	8.4	8.0

This can be explained, at least in part, by the heating of the PEM electrolyser. By switching from 25 °C to 50 °C, the performance of the PEM electrolyser (biased at a fixed voltage of 1.50 V, in the dark) was improved, as shown in Fig. 2c. At 50 °C, an operating current (I_{op}) of 800 mA and a corresponding hydrogen flow rate of 6 mL min^{-1} were obtained, compared to 250 mA and 2 mL min^{-1} at 25 °C. Moreover, under 1 sun, with no external heating other than the illumination source, the operating current stabilized close to 1 A with a hydrogen flow rate of around 8 mL min^{-1}. This is likely due to the more homogeneous heating achieved by the uniform surface irradiation than by the hot water flow alone. The slight shift in operating voltage (V_{op}) with heating (decreasing from 1.49 to 1.44 V) is also consistent with the PEM electrolyser operating at a higher temperature. The faradaic efficiency (FE) is 74% on average (see Table S3†) in the IPEC cell compared to more than 98% in the PEM electrolyser (dark) at 1.5 V. The reason for this might be linked to the current value, which was ten times lower in the IPEC cells than for the PEM electrolysers measured in the dark (see Fig. 2c and d). Lower operating currents have been reported to favour gas crossover through the membrane, and consequently, decrease faradaic efficiency, as modelled by Schalenbach *et al.*[37]

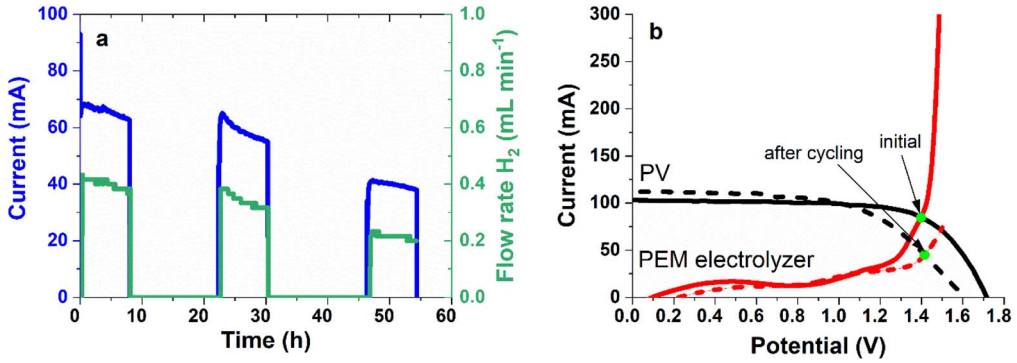

Fig. 3 IPEC cell stability in light/dark cycles. (a) Operating current (in blue) and hydrogen flow rate (in green). (b) $I(V)$ curves of the PEM electrolyser (red) and of the tandem solar cell (black) before (plain) and after (dashed) the three 8 h-long illumination cycles.

We systematically observed the positive impact of the thermal integration on IPEC cell performance (see Table S4†), although the STH efficiency did not always strictly reach the same value. This could be explained by the dispersion in the $I(V)$ shape of the solar cells. On a batch of fourty five solar cells, we recorded some variations in the $I(V)$ curves, particularly in the area of the crossing point with the PEM electrolyser curve. This resulted in some dispersion of the expected STH efficiency, calculated from the current delivered by the tandem solar cells at 1.45 V (and taking a constant FE of 74%). The calculated STH efficiency ranged from 7.5 to 10.8% (see Fig. S7†).

3.3 IPEC cell stability and efficiency under cyclic light (1 sun)–dark illumination

The stability of the IPEC cells under cyclic 1 sun illumination was evaluated, following the so-called ISOS-LC-1 protocol from the perovskite photovoltaics community,[38] but with the solar cell delivering its power to the electrolyser. We performed 8 hour light cycles, followed by a recovery time of at least 16 h in the dark. A slow decay in operating current was systematically observed under illumination (Fig. 3a and S8†). The behaviour during recovery in the dark is different for cycles 1–2 and 2–3. In both experiments, while the starting point of cycle 2 stands at the ending point of cycle 1, the starting point of cycle 3 is lower than the ending point of cycle 2, as if the cells were degrading in the dark. This could indicate that different degradation modes occur initially and after the second cycle.

The $I(V)$ curves of each component of the IPEC were compared before/after the three light cycles (Fig. 3b). Significant degradation was observed for the solar cell; open circuit voltage (V_{oc}), fill factor and series resistance are markedly affected, possibly indicating a degradation in the perovskite material and its interface layers (ETL and HTL). The increase in current produced by the tandem solar cell close to short circuit could originate from a shunted perovskite subcell and/or from the change in current balance due to perovskite material degradation. As the perovskite/silicon tandem solar cell is the least mature component of the IPEC cell, it is not surprising that it is the least stable.

In order to optimize the operating current I_{op}, we adjusted the perovskite thickness to be in a bottom-limited configuration (providing a better fill factor). But as the perovskite material degrades, this may no longer be true, and shunts in the perovskite top cell may appear on the $I(V)$ curve, with a slope impacting the short-circuit current. Regarding the PEM electrolyser, the $I(V)$ curve shifts towards higher potentials (reflecting an increase in resistance, overpotential and/or mass transport limitations). The mechanisms at the origin of this phenomenon have to be further investigated (starting with a study of membrane degradation over time). Overall, the expected operating point is shifted toward lower current, which is consistent with the experimental results. The performance of the IPEC cell under cyclic light (1 sun)–dark illumination is compared in Table 2. STH efficiency drops to half of its initial value after three 8 h illumination cycles, from 8.6 to 4.5%, in accordance with the observations from Fig. 3b.

3.4 IPEC module efficiency

Fig. 4a shows an exploded view of water circulation in the module. Cold water (T_1) enters the heat exchanger (cathodic plate) of each IPEC successively and gradually heats up until it reaches its maximal temperature at the outlet of the last IPEC

Table 2 Performance of the IPEC cell over three cycles of 8 h under 1 sun (inlet water temperature: 25 °C, V_{op} and I_{op}: operating voltage and current recorded at the electrolyser's terminals, t: duration of the hydrogen production, vol. H_2: corresponding hydrogen produced during the experiments of Fig. 3, and STH and STH*: solar-to-hydrogen efficiencies calculated using two methods as described in the Materials and methods section)

Cycle	V_{op} (V)	Average I_{op} (mA)	t (h)	Vol. H_2 (L)	STH (%)	STH* (%)
1	From 1.45 to 1.53	66	8	0.19	8.6	8.6
2		59	8	0.16	7.2	7.2
3		40	8	0.10	4.5	4.4

cathode. The preheated water flow (T_2) is then divided into three identical flows, each passing through a series of three anodes, where it is oxidized to O_2 and protons. The reason for dividing the water flow into three equal parts is to limit the overvoltage potentially associated with the accumulation of O_2 bubbles.[39]

Fig. 4b shows that the heat exchanger of the IPEC module under 1 sun operates in the same way as that of the IPEC cell. The temperatures stabilize at values comparable to those for the IPEC cell (Fig. 2b): close to 60 °C for the tandem solar cells (T_6) and 50 °C for the water in the anodic compartment of the PEM electrolyser (T_3). Fig. 4c shows the operating currents of the nine IPEC cells constituting the IPEC module, initially and during a 6 hour stability test under continuous 1 sun illumination (see details in Table S5†). Initial operating currents range from 24 to 57 mA and are lower than those observed for the IPEC cell (70 mA, Table 1), which can be explained by the already marked ageing of the tandem solar cells used in previous experiments. Under these conditions, according to the measured currents, the IPEC module delivers an estimated amount of 552 mL of hydrogen in 6 h, corresponding to a hydrogen flow rate of around 2 mL min^{-1} (Fig. 4d).

The corresponding STH efficiencies are reported in Table 3. Assuming a constant FE of 74%, the measured currents result in a STH efficiency of 3.7%, about two times less than what would be expected from nine fresh and stable IPEC cells (as in Table 1). Therefore, the volume of H_2 produced by the best achievable IPEC module (made with nine fresh tandem solar cells) could reach 1.21 L over 6 h under 1 sun.

3.5 IPEC module stability outdoors and origin of degradation

Several IPEC modules were tested in an autonomous device dedicated to the production of green methane.[31] The conditions of this 72 hour demonstration, conducted at the JRC center in Ispra,¶ differ significantly from the laboratory tests described previously on several major points.

First, the modules had to operate under real sunlight and climate conditions (ISOS-O-1 protocol[38]). They all shared the same water inlet and hydrogen outlet circuits. In addition, they were coupled to a bioreactor carrying out the continuous conversion of CO_2 with "as produced" H_2 into green methane (without any compression, heating or storage step prior to use).[40] Consequently, the H_2 flow at the IPEC outlet was regulated using a control system that only allows H_2 to evacuate above a pressure of 20 mbar.[31]

The device was sized for an average hydrogen conversion capacity of 0.5 L h^{-1} (8 mL min^{-1}). To this end, we assembled five IPEC modules, capable of delivering around 16 mL min^{-1} of H_2 initially, based on the data reported in Table 1 and taking into account the effect of aging. Fourty five tandem solar cells were selected within several batches, the selection criterion being the current delivered by the solar cell under 1 sun at a given fixed voltage of 1.45 V (close to the operating point). This value stands a few tens of mV above the typical maximum power point of n–i–p perovskite/silicon tandem solar cells under 1 sun (see Fig. S5†), in a region where the $I(V)$ curve follows an exponential shape, with a steep slope. To improve this current (increase the maximum power point voltage), we modified the parameters of certain batches, adjusting the concentration of the perovskite solution (from 1.2 to 1.4 mol L^{-1}, see Fig. S9†) to increase the thickness of the perovskite layer and shift the tandem into a bottom cell limited configuration. The p-layer concentration (PTAA solution) was also increased from 6 to 12 g L^{-1} as it led to a slightly better maximum power point voltage (see Fig. S9†). Unfortunately, such improvements were lost once the tandems were encapsulated: the current values delivered by the solar cells at 1.45 V after encapsulation were all in the same range, as displayed in Fig. 5b (blue points). The mechanical stress linked to crosslinking of the glue, imposing stress on the interfaces, could be a clue to explain this result,[41] as an increased series resistance was observed after encapsulation.

Fig. 5a presents the volume of hydrogen produced by the five IPEC modules over time and the corresponding irradiance. As hydrogen is measured close to the bioreactor inlet, significant dead volumes have to be taken into account, which explains the delay between irradiance onset and hydrogen detection. In total, around 7 L of hydrogen were evolved by the five IPEC modules over the 72 h test. For comparison with the previous ageing cycles performed under simulated 1 sun conditions, production periods with steady hydrogen production were selected (Fig. 5a). The corresponding volumes, reported for an 8 hour period, per module, for the production periods indicated in Fig. 5a, are reported in Table 4. They are consistent with the values observed for the IPEC module comprising aged tandems from Fig. 4 and Table 3 (0.55 L in 6 h). Thus, between 0.66 and 0.72 L of hydrogen were produced by each module in 8 h, under natural illumination with an irradiance of several hundreds of watts per square meter. The corresponding STH* values are reported in Table 4 and range between 3.8 and 9.3%, depending on the outdoor conditions. Overall, the STH* from the whole 72 hour outdoor test for the five IPEC modules was 6.3%.

Fig. 5b shows the evolution of the current of the tandem solar cells at 1.45 V under 1 sun (representative of the operating current) before and after outdoor ageing. To obtain these values, we disconnected the tandem solar cells from the IPEC modules and characterized them under a calibrated solar simulator. While variations in perovskite and PTAA thickness led to devices with initial current values in the same range, the highest current losses observed after ageing occur in the case of the thickest p-layer. The analysis of the $I(V)$ curves indicates that degradation results in an increase in open-circuit resistance and a reduction of the fill factor (Fig. S10 and S11†). As the open-circuit voltage remains stable, the perovskite material is not degraded. Thus, the degradation of the tandem solar cell seems to originate at the perovskite/p-layer interface or within the p-layer.

The tandem solar cells were encapsulated with glass and a glue with high gas barrier properties, and hence the main stress factors affecting them during outdoor ageing should be

¶ European Commission, Directorate-General for Research and Innovation, Fuel from the Sun: Artificial Photosynthesis – EIC Horizon Prize – Commissariat à l'énergie atomique et aux énergies alternatives (CEA), Publications Office of the European Union, 2022, https://data.europa.eu/doi/10.2777/18380

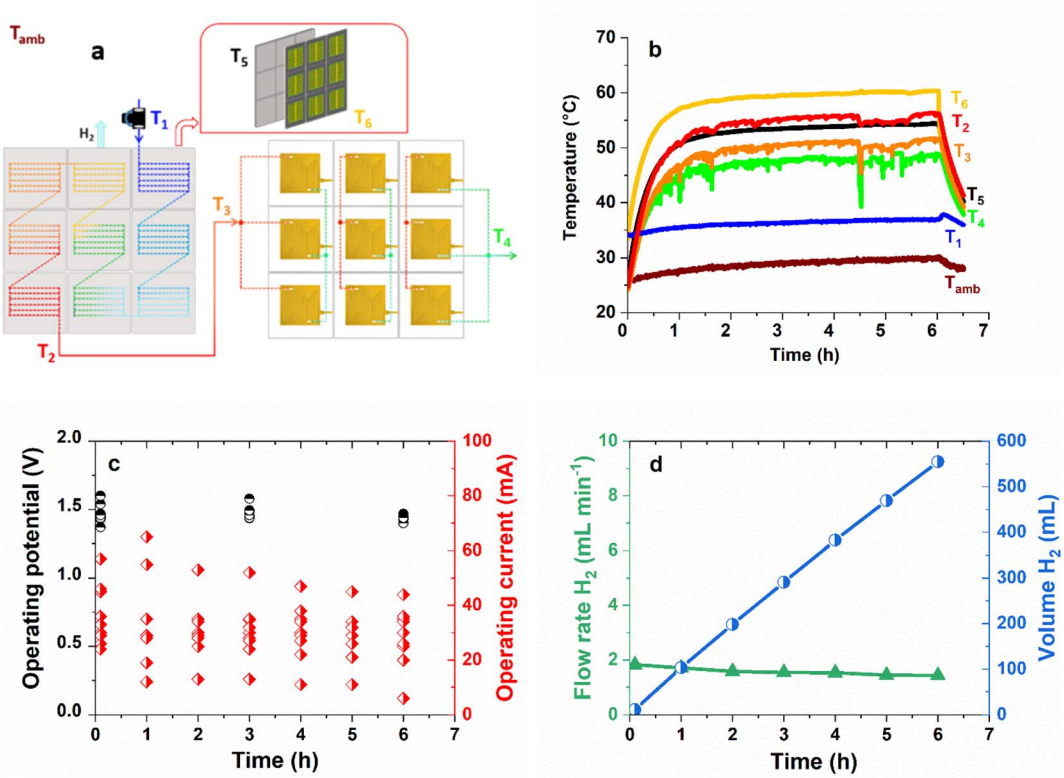

Fig. 4 IPEC module thermal integration and performance (68.4 cm^2 active area). (a) Detailed scheme of the water circuit in the IPEC module and (b) recorded temperatures. T_{amb}: ambient temperature. T_1 (blue): water inlet in the heat exchanger. T_2 (red): water outlet from the heat exchanger. T_3 (red): water inlet in the anodic compartment. T_4 (green): water outlet from the anodic compartment. T_5 (black): temperature of the cathodic plate. T_6 (yellow): temperature of the tandem solar cell. (c) Operating points (V_{op} and I_{op}) of the nine IPEC cells in the IPEC module before and during constant 1 sun illumination. (d) Calculated H_2 volume and flow rate produced by the IPEC module.

Table 3 Performance of the IPEC module (68.4 cm^2 active area) over 6 h under 1 sun (inlet water temperature: 25 °C, average I_{op}: average I_{op} recorded at each electrolyser's terminals over 6 h, t: duration of the hydrogen production, vol. H_2: corresponding calculated hydrogen produced during the experiments of Fig. 4, and STH and STH*: solar-to-hydrogen efficiencies calculated as described in the Materials and methods section). Values for the best expected IPEC module (consisting of 9 fresh and stable IPEC cells) are also given

	Average I_{op} (mA)	t (h)	Calculated vol. H_2 (L)	STH (%)	Estimated STH* (%)
IPEC module from Fig. 4	282	6	0.56	3.7	3.6
9 IPEC cells as in Table 1	630 (70 × 9)	6	1.21 (~0.13 × 9)	8.3	8.0

light, heat, their combination and cycling. From our previous experience, we did observe moisture ingress, which quickly made the tandem edges turn yellow due to perovskite decomposition, but only after heavy rain. Here, devices are more likely affected by illumination and thermal stress.

Some studies report the thermal oxidation and morphological changes in PTAA thin films (aged at 65 °C in air)[42] that could potentially induce lower conductivity and impact the fill factor when integrated into solar cells. Delamination at interfaces due to thermal expansion coefficient mismatch was also reported.[43] Yaghoobi Nia *et al.* studied the thermal stability of n–i–p perovskite solar cells with doped PTAA and highlighted the impact of PTAA molecular weight and doping on device stability, through modification of the passivation of the perovskite/p-layer interface.[44] Similarly, Rombach *et al.*[43] assigned the degradation of n–i–p perovskite solar cells to PTAA doping, which affects the perovskite/PTAA interface. Therefore, our assumption that the solar cells degrade at the perovskite/p-layer interface or within the p-layer is consistent with previous detailed investigations on similar devices. Better stability could be reached by tuning the tandem interfaces and performing in-depth analysis of the degradation pathways.

4 Comparison with state-of-the-art

Fig. 6 and Table S6† show the performance of the devices from this study compared with the largest and most efficient solar hydrogen production systems selected from the literature.

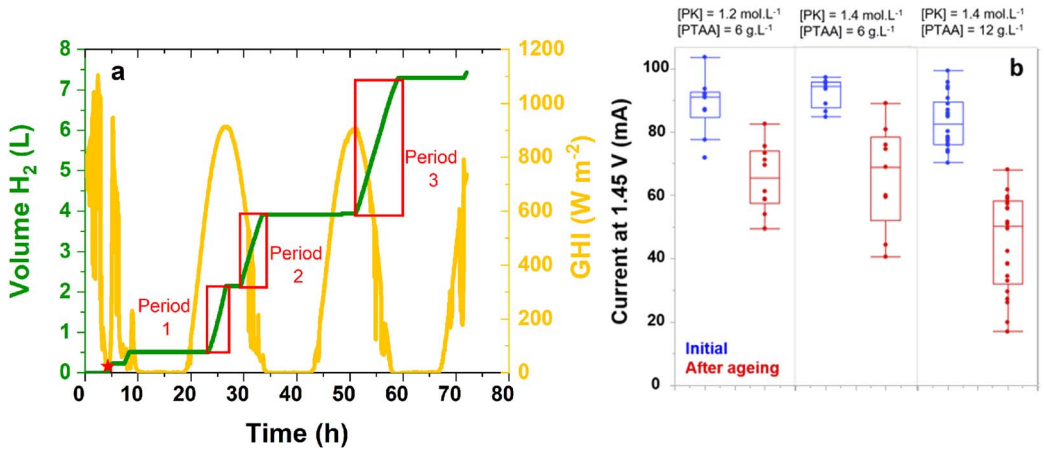

Fig. 5 Outdoor functioning of five IPEC modules (342 cm^2 active area). (a) Evolved hydrogen (in red) and corresponding Global Horizontal Irradiance (GHI, in orange) recorded in the field. Three periods (shown in red) were selected for STH efficiency calculations. (b) Current delivered by the tandem solar cells at 1.45 V under 1 sun: before (blue) and after outdoor ageing (red), from batches with variations in perovskite top cell conditions (perovskite and p-layer concentrations). To perform these measurements, the solar cells were dismounted from the IPEC modules and measured under a calibrated solar simulator.

Today, the largest systems deployed are using mature and abundant silicon-based absorbers. However, such systems have an intrinsic efficiency limitation due to the single junction optical absorption.[22] The maximum reported STH efficiencies so far are close to 15%. Alternately, large-scale devices can be obtained with cheap abundant photocatalysts (PCs). Their lower efficiency, in the range of a few percent, is mitigated by the possibility of scaling-up the system. The use

Table 4 Amount of hydrogen produced outdoors by each IPEC module, measured over real periods (shown in red in Fig. 5) and calculated for 8 hour periods for comparison with IPEC cell data. The total amount of hydrogen produced by the five IPEC modules over the 72 hour test is also reported. STH* values are calculated from the measured hydrogen volumes and corrected global horizontal irradiance, as explained in the Materials and methods section

	Calculated vol. H_2 (L) for 8 h	Measured vol. H_2 (L)	STH* (%)
Period 1 Average irradiance 850 W m^{-2}	0.72	0.33	3.8
Period 2 Average irradiance 297 W m^{-2}	0.62	0.33	9.3
Period 3 Average irradiance 389 W m^{-2}	0.66	0.64	7.6
72 hour outdoor test, 5 IPEC modules (342 cm^2)	—	7.43	6.3 (without GHI correction: 7.0%)

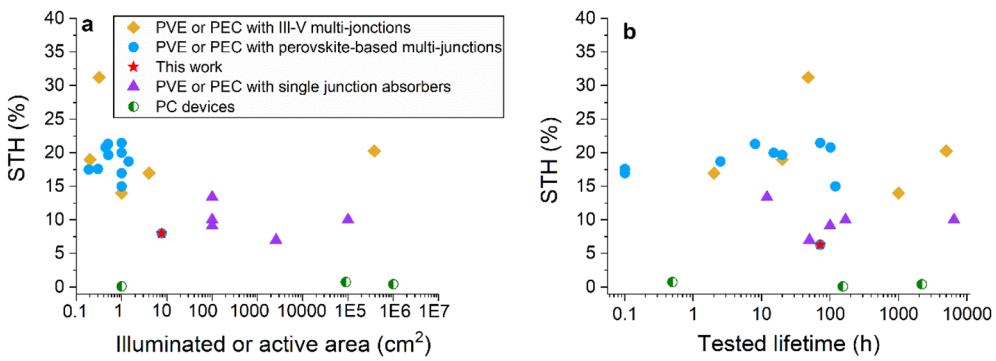

Fig. 6 Performance of selected reports from the literature regarding photocatalytic systems (PCs), photovoltaic cells coupled to electrolysers (PVEs), photoelectrochemical cells and integrated photoelectrochemical cells (PECs and IPECs), with single junction absorbers (silicon or CIGS), multi-junctions (with III–V absorbers), and perovskite-based tandems. (a) STH efficiency as a function of absorber active area. (b) STH efficiency and tested lifetime (results gathered under various ageing conditions: light cycling, continuous illumination or outdoor). The red stars correspond to the devices from this study: IPEC cells from Table 1 (7.6 cm^2 and 8% STH*) and IPEC modules aged outdoors (342 cm^2 and 6.3% STH*) from Table 4.

of PC inorganic metal oxide particles, in slurry form or deposited onto solid substrates, has demonstrated long-term stability and scale-up potential (with a recent demonstration of over 100 m^2).[45] However, this type of device has so far been limited to a low STH efficiency and requires downstream separation of O_2 and H_2.[46]

The US Department of Energy (DoE) recommends and targets STH efficiencies of at least 20% for systems to be commercially viable.[47] This motivated the development of multi-junction water splitting devices. Today, the most efficient way to produce solar hydrogen, with up to 30% STH efficiency, is through the combination of III–V absorbers in a multi-junction cell connected with electrolysers and using light concentration. This mature technology guarantees high performance[48] but it is associated with high investment costs.[49] A monolithic buried junction device using the same high efficiency high-cost components reaches a STH efficiency of 19%, but with lower stability because of the corrosion of III–V semiconductor materials in contact with liquid electrolytes.[50,51] Such multi-junctions were used in kilowatt scale devices by Holmes-Gentle *et al.*[11] Perovskite-based multi-junctions have shown high STH efficiency (over 20%) at a potentially low cost. However, no data is available beyond 1.42 cm^2. Here, we have demonstrated that larger photoelectrochemical devices can be obtained using larger perovskite/silicon tandems (7.6 cm^2) and up to 342 cm^2 through a numbering-up approach. It should be noted that there is no technological obstacle to adapting this strategy to larger cells, such as the ones recently reported.[52]

Higher STH efficiencies could have been obtained if the operating point of the IPEC cells had perfectly matched the maximum power point of the solar cells, which was not the case here, contrary to previous work from the literature. Indeed, although we adjusted the perovskite and PTAA layers, the initial gains obtained at the maximum power point could not be translated into the encapsulated tandems, probably due to the mechanical stress arising from the adhesive crosslinking. In fact, today, the record power conversion efficiencies of perovskite/silicon tandems are obtained with p–i–n architectures, probably due to the better quality of the interfaces that can be achieved with the materials implemented in such architectures (self-assembled monolayers, buffer layers…). We expect that the combination of p–i–n-based architectures with optimized encapsulation and more efficient heat transfer will show significant progress in STH efficiency.[53] Progress towards the commercialization of solar panels made of perovskite/silicon tandem cells[54] will undoubtedly help in this direction.

5 Conclusions and prospects

In conclusion, this work not only demonstrates results regarding the scaling up of perovskite-based integrated photoelectrochemical devices and their lifetime assessment in a real environment, but also provides an example of a modular and scalable system that enables rapid testing and characterization of components, thanks to reversible integration. Additive manufacturing has enabled the implementation in a single component of the gas collection function and a heat exchanger.

This study confirms the benefits of thermal integration in improving STH efficiency, obtaining almost doubled values with the embedded heat exchanger in direct contact with the back side of the solar cell. With a more efficient thermal transfer, effectively cooling the solar cell, even better results could be achieved.

Our study provides noteworthy insights into the practical deployment of integrated photoelectrochemical devices. We collected repeatability data on over fourty-five IPEC cells, showing the expected scatter in STH efficiencies due to variability in solar cell $I(V)$ curves. The modular approach presented here enabled us to rapidly scale-up the device to an active surface area of 342 cm^2 , even though individual components remained on a scale of a few cm^2. The development of larger components, and especially of tandem solar cells,[54] will also directly contribute to upscaling the IPEC devices. This numbering up strategy is in line with the recent concept of golden hydrogen for adaptable and decentralized hydrogen production units.[8]

The approach presented here paves the way for further investigations of other promising materials, such as light absorbers, electrocatalysts, or membranes, in order to compare performance, stability, and repeatability, and to highlight the limitations of such new systems.

Data availability

The data supporting this article have been included as part of the ESI.†

Author contributions

MM, VA and SC conceived the project. ARAM, AM, JF, MP, MM and SC performed the experimental work. ARAM, AM, MM, SC and VA analyzed data and wrote the manuscript.

Conflicts of interest

Some of the authors filed patent applications listed in the references.

Acknowledgements

This work was partially supported by Carnot Energies du Futur, the Agence Nationale de la Recherche (ANR) for projects Labex ARCANE and CBH-EUR-GS (ANR-17-EURE-0003), the DRF-Impulsion program and the ECC inflexion program of the Fundamental Research Division of CEA, and by the Carbon Circular Economy Program of the Energies Division of CEA. The authors thank the Tandem Cells Laboratory at CEA LITEN at INES for providing the tandem cells, Frédéric Fouda-Onana and Nicolas Guillet (LITEN) for their advice on PEM electrolysers, Grégory Cwicklinski, Michel Boujard and Eric Delamadeleine (IRIG) as well as Guilhem Roux (LITEN) for their technical support, Jean-Marc Borgard (ISAS) for techno-economic analyses and Hervé Bercegol (IRAMIS) for his continuous support during the project. The authors would also like to thank the

local organization team of the Horizon Prize Grand Finale at JRC Ispra for their welcome and for providing the irradiation data.

References

1 M. G. Walter, E. L. Warren, J. R. McKone, S. W. Boettcher, Q. Mi, E. A. Santori, *et al.*, Solar water splitting cells, *Chem. Rev.*, 2010, **110**(11), 6446–6473.
2 S. Tembhurne and S. Haussener, Integrated Photo-Electrochemical Solar Fuel Generators under Concentrated Irradiation, *J. Electrochem. Soc.*, 2016, **163**(10), H999–H1007.
3 B. A. Pinaud, J. D. Benck, L. C. Seitz, A. J. Forman, Z. Chen, T. G. Deutsch, *et al.*, Technical and Economic Feasibility of Centralized Facilities for Solar Hydrogen Production via Photocatalysis and Photoelectrochemistry, *Energy Environ. Sci.*, 2013, **6**(7), 1983.
4 B. D. James, G. N. Baum, J. Perez and K. N. Baum, *Technoeconomic Analysis of Photoelectrochemical (PEC) Hydrogen Production, Final Report*, 2009 Dec [cited 2024 Feb 29], Report No.: 1218403, available from: **http://www.osti.gov/servlets/purl/1218403/**.
5 T. Grube, J. Reul, M. Reuß, S. Calnan, N. Monnerie, R. Schlatmann, *et al.*, A techno-economic perspective on solar-to-hydrogen concepts through 2025, *Sustainable Energy Fuels*, 2020, **4**(11), 5818–5834.
6 A. Sharma, T. Longden, K. Catchpole and J. Beck F, Comparative techno-economic analysis of different PV-assisted direct solar hydrogen generation systems, *Energy Environ. Sci.*, 2023, **16**(10), 4486–4501.
7 Net Zero Roadmap: A Global Pathway to Keep the 1.5 °C Goal in Reach – 2023 Update.
8 F. Lubbe, J. Rongé, T. Bosserez and J. A. Martens, Golden hydrogen, *Curr. Opin. Green Sustainable Chem.*, 2023, **39**, 100732.
9 J. H. Kim, D. Hansora, P. Sharma, J. W. Jang and J. S. Lee, Toward practical solar hydrogen production – an artificial photosynthetic leaf-to-farm challenge, *Chem. Soc. Rev.*, 2019, **48**(7), 1908–1971.
10 T. A. Kistler, G. Zeng, J. L. Young, L. C. Weng, C. Aldridge, K. Wyatt, *et al.*, Emergent Degradation Phenomena Demonstrated on Resilient, Flexible, and Scalable Integrated Photoelectrochemical Cells, *Adv. Energy Mater.*, 2020, **10**(48), 2002706.
11 I. Holmes-Gentle, S. Tembhurne, C. Suter and S. Haussener, Kilowatt-scale solar hydrogen production system using a concentrated integrated photoelectrochemical device, *Nat. Energy*, 2023, **8**(6), 586–596.
12 E. Aydin, E. Ugur, B. K. Yildirim, T. G. Allen, P. Dally, A. Razzaq, *et al.*, Enhanced optoelectronic coupling for perovskite/silicon tandem solar cells, *Nature*, 2023, **623**(7988), 732–738.
13 H. Park, I. J. Park, M. G. Lee, K. C. Kwon, S. P. Hong, D. H. Kim, *et al.*, Water Splitting Exceeding 17% Solar-to-Hydrogen Conversion Efficiency Using Solution-Processed Ni-Based Electrocatalysts and Perovskite/Si Tandem Solar Cell, *ACS Appl. Mater. Interfaces*, 2019, **11**(37), 33835–33843.
14 J. Gao, F. Sahli, C. Liu, D. Ren, X. Guo, J. Werner, *et al.*, Solar Water Splitting with Perovskite/Silicon Tandem Cell and TiC-Supported Pt Nanocluster Electrocatalyst, *Joule*, 2019, **3**(12), 2930–2941.
15 S. K. Karuturi, H. Shen, A. Sharma, F. J. Beck, P. Varadhan, T. Duong, *et al.*, Over 17% Efficiency Stand-Alone Solar Water Splitting Enabled by Perovskite-Silicon Tandem Absorbers, *Adv. Energy Mater.*, 2020, **10**(28), 1–9.
16 Y. Wang, A. Sharma, T. Duong, H. Arandiyan, T. Zhao, D. Zhang, *et al.*, Direct Solar Hydrogen Generation at 20% Efficiency Using Low-Cost Materials, *Adv. Energy Mater.*, 2021, **11**(34), 2101053.
17 M. Wang, B. Shi, Q. Zhang, X. Li, S. Pan, Y. Zhao, *et al.*, Integrated and Unassisted Solar Water-Splitting System by Monolithic Perovskite/Silicon Tandem Solar Cell, *Sol. RRL*, 2022, **6**(2), 2100748.
18 S. Pan, R. Li, Q. Zhang, C. Cui, M. Wang, B. Shi, *et al.*, An over 20% solar-to-hydrogen efficiency system comprising a self-reconstructed NiCoFe-based hydroxide nanosheet electrocatalyst and monolithic perovskite/silicon tandem solar cell, *J. Mater. Chem. A*, 2021, **9**(24), 14085–14092.
19 K. Datta, B. Branco, Y. Zhao, V. Zardetto, N. Phung, A. Bracesco, *et al.*, Efficient Continuous Light-Driven Electrochemical Water Splitting Enabled by Monolithic Perovskite-Silicon Tandem Photovoltaics, *Adv. Mater. Technol.*, 2023, **8**(2), 2201131.
20 A. M. K. Fehr, A. Agrawal, F. Mandani, C. L. Conrad, Q. Jiang, S. Y. Park, *et al.*, Integrated halide perovskite photoelectrochemical cells with solar-driven water-splitting efficiency of 20.8%, *Nat. Commun.*, 2023, **14**(1), 3797.
21 Y. H. Chiu, T. H. Lai, M. Y. Kuo, P. Y. Hsieh and Y. J. Hsu, Photoelectrochemical cells for solar hydrogen production: Challenges and opportunities, *APL Mater.*, 2019, **7**, 80901.
22 H. Döscher, J. F. Geisz, T. G. Deutsch and J. A. Turner, Sunlight absorption in water – efficiency and design implications for photoelectrochemical devices, *Energy Environ. Sci.*, 2014, **7**(9), 2951–2956.
23 A. M. K. Fehr, T. G. Deutsch, F. M. Toma, M. S. Wong and A. D. Mohite, Technoeconomic Model and Pathway to <$2/kg Green Hydrogen Using Integrated Halide Perovskite Photoelectrochemical Cells, *ACS Energy Lett.*, 2023, 4976–4983.
24 S. Tembhurne, F. Nandjou and S. Haussener, A thermally synergistic photo-electrochemical hydrogen generator operating under concentrated solar irradiation, *Nat. Energy*, 2019, **4**(5), 399–407.
25 S. Calnan, R. Bagacki, F. Bao, I. Dorbandt, E. Kemppainen, C. Schary, *et al.*, Development of Various Photovoltaic-Driven Water Electrolysis Technologies for Green Solar Hydrogen Generation, *Sol. RRL*, 2022, **6**(5), 2100479.
26 K. Welter, V. Smirnov, J. P. Becker, P. Borowski, S. Hoch, A. Maljusch, *et al.*, The Influence of Operation Temperature and Variations of the Illumination on the Performance of Integrated Photoelectrochemical Water-Splitting Devices, *ChemElectroChem*, 2017, **4**(8), 2099–2108.
27 A. C. Lourenço, A. S. Reis-Machado, E. Fortunato, R. Martins and M. J. Mendes, Sunlight-driven CO2-to-fuel conversion: Exploring thermal and electrical coupling between

photovoltaic and electrochemical systems for optimum solar-methane production, *Mater. Today Energy*, 2020, **17**, 100425.
28 Q. Jiang, R. Tirawat, R. A. Kerner, E. A. Gaulding, Y. Xian, X. Wang, *et al.*, Towards linking lab and field lifetimes of perovskite solar cells, *Nature*, 2023, **623**(7986), 313–318.
29 M. Pellat, G. Roux, A. R. A. Maragno, S. Charton, V. Artero and M. Matheron, Photoelectrochemical converter for producing dihydrogen, WO2023057374, 2023.
30 M. Pellat, G. Roux, S. Charton and A. R. A. Maragno, Photoelectrochemical converter for producing dihydrogen, WO 2023057376, 2023.
31 A. R. A. Maragno, G. Cwicklinski, M. Matheron, R. Vanoorenberghe, J.-M. Borgard, A. Morozan, J. Fize, M. Pellat, C. Cavazza, V. Artero and S. Charton, A scalable integrated solar device for the autonomous production of green methane, *Joule*, 2024, **8**, 1–17.
32 C. Y. Lee, A. C. Taylor, A. Nattestad, S. Beirne and G. G. Wallace, 3D Printing for Electrocatalytic Applications, *Joule*, 2019, **3**(8), 1835–1849.
33 G. Yang, J. Mo, Z. Kang, Y. Dohrmann, F. A. List, J. B. Green, *et al.*, Fully printed and integrated electrolyzer cells with additive manufacturing for high-efficiency water splitting, *Appl. Energy*, 2018, **215**, 202–210.
34 W. M. Haynes, CRC Handbook of Chemistry and Physics. 2014th–2015th ed. Haynes WM, Lide DR, editors, *J. Am. Pharm. Assoc.*, 2015, 3–488.
35 Integrated Solar Fuel Generators. The Royal Society of Chemistry; 2018 [cited 2024 Feb 24], available from: **https://books.rsc.org/books/edited-volume/1835/Integrated-Solar-Fuel-Generators**.
36 G. Chisholm, P. J. Kitson, N. D. Kirkaldy, L. G. Bloor and L. Cronin, 3D printed flow plates for the electrolysis of water: An economic and adaptable approach to device manufacture, *Energy Environ. Sci.*, 2014, **7**(9), 3026–3032.
37 M. Schalenbach, M. Carmo, D. L. Fritz, J. Mergel and D. Stolten, Pressurized PEM water electrolysis: Efficiency and gas crossover, *Int. J. Hydrogen Energy*, 2013, **38**(35), 14921–14933.
38 M. V. Khenkin, E. A. Katz, A. Abate, G. Bardizza, J. J. Berry, C. Brabec, *et al.*, Consensus statement for stability assessment and reporting for perovskite photovoltaics based on ISOS procedures, *Nat. Energy*, 2020, **5**(1), 35–49.
39 H. Vogt and R. J. Balzer, The bubble coverage of gas-evolving electrodes in stagnant electrolytes, *Electrochim. Acta*, 2005, **50**(10), 2073–2079.
40 G. Cwicklinski, R. Miras, J. Pérard, C. Rinaldi, E. Darrouzet and C. Cavazza, Development of a CO_2-biomethanation reactor for producing methane from green H_2, *Sustainable Energy Fuels*, 2024, **8**, 1068–1076, available from: **https://pubs.rsc.org/en/content/articlelanding/2024/se/d3se01550e**.
41 S. Juillard, E. Planes, M. Matheron, L. Perrin, S. Berson and L. Flandin, Mechanical Reliability of Flexible Encapsulated Organic Solar Cells: Characterization and Improvement, *ACS Appl. Mater. Interfaces*, 2018, **10**(35), 29805–29813.
42 M. Sendner, J. Trollmann and A. Pucci, Dielectric function and degradation process of poly(triarylamine) (PTAA), *Org. Electron.*, 2014, **15**(11), 2959–2963.
43 F. M. Rombach, S. A. Haque and T. J. Macdonald, Lessons learned from spiro-OMeTAD and PTAA in perovskite solar cells, *Energy Environ. Sci.*, 2021, **14**(10), 5161–5190.
44 N. Yaghoobi Nia, M. Zendehdel, M. Abdi-Jalebi, L. A. Castriotta, F. U. Kosasih, E. Lamanna, *et al.*, Beyond 17% stable perovskite solar module via polaron arrangement of tuned polymeric hole transport layer, *Nano Energy*, 2021, **82**, 105685.
45 H. Nishiyama, T. Yamada, M. Nakabayashi, Y. Maehara, M. Yamaguchi, Y. Kuromiya, *et al.*, Photocatalytic solar hydrogen production from water on a 100-m2 scale, *Nature*, 2021, **598**(7880), 304–307.
46 Y. Goto, T. Hisatomi, Q. Wang, T. Higashi, K. Ishikiriyama, T. Maeda, *et al.*, A Particulate Photocatalyst Water-Splitting Panel for Large-Scale Solar Hydrogen Generation, *Joule*, 2018, **2**(3), 509.
47 E. L. Miller, Photoelectrochemical water splitting, *Energy Environ. Sci.*, 2015, **8**, 2809.
48 Z. N. Zahran, Y. Miseki, E. A. Mohamed, Y. Tsubonouchi, K. Makita, T. Sugaya, *et al.*, Perfect Matching Factor between a Customized Double-Junction GaAs Photovoltaic Device and an Electrolyzer for Efficient Solar Water Splitting, *ACS Appl. Energy Mater.*, 2022, **5**(7), 8241–8253.
49 Z. N. Zahran, Y. Tsubonouchi and M. Yagi, Solar-Driven H2 Production in PVE Systems, *Sol Fuels*, 2023, 341–373.
50 S. Y. Reece, J. A. Hamel, K. Sung, T. D. Jarvi, A. J. Esswein, P. null, *et al.*, Wireless Solar Water Splitting Using Silicon-Based Semiconductors and Earth-Abundant Catalysts, *Science*, 2011, **334**(6056), 645.
51 W. H. Cheng, M. H. Richter, M. M. May, J. Ohlmann, D. Lackner, F. Dimroth, *et al.*, Monolithic Photoelectrochemical Device for Direct Water Splitting with 19% Efficiency, *ACS Energy Lett.*, 2018, **3**(8), 1795–1800.
52 G. Yang, Z. J. Yu, M. Wang, Z. Shi, Z. Ni, H. Jiao, *et al.*, Shunt mitigation toward efficient large-area perovskite-silicon tandem solar cells, *Cell Rep. Phys. Sci.*, 2023, **4**(10), 101628.
53 S. Charton, A. R. A. Maragno, M. Matheron and V. Artero, Convertisseur photoélectrochimique, FR2313467, 2023.
54 E. Aydin, T. G. Allen, M. D. Bastiani, A. Razzaq, L. Xu, E. Ugur, *et al.*, Pathways toward commercial perovskite/silicon tandem photovoltaics, *Science*, 2024, **383**(6679), eadh3849.